Critical behavior in 3D gravitational collapse of massless scalar fields

Nils Deppe,[1,*] Lawrence E. Kidder,[1] Mark A. Scheel,[2] and Saul A. Teukolsky[1,2]

[1]*Cornell Center for Astrophysics and Planetary Science, Cornell University, Ithaca, New York 14853, USA*
[2]*Theoretical Astrophysics 350-17, California Institute of Technology, Pasadena, California 91125, USA*

We present results from a study of critical behavior in 3D gravitational collapse with no symmetry assumptions. The source of the gravitational field is a massless scalar field. This is a well-studied case for spherically symmetric gravitational collapse, allowing us to understand the reliability and accuracy of the simulations. We study both supercritical and subcritical evolutions to see if one provides more accurate results than the other. We find that even for nonspherical initial data with 35% of the power in the $\ell = 2$ spherical harmonic, the critical solution is the same as in spherical symmetry.

I. INTRODUCTION

Critical behavior in the gravitational collapse of a massless scalar field was discovered by Choptuik [1], who sought to answer the question "What happens at the threshold of black hole formation?" Choptuik considered a massless scalar field undergoing gravitational collapse in a spherically symmetric spacetime. He found that for some parameter p in the initial data, for example the amplitude of a Gaussian-distributed scalar field, the final mass of the black hole is related to p by

$$M_{\rm BH} \propto \left| \frac{p}{p_\star} - 1 \right|^{\gamma_M}. \tag{1}$$

Here $p_\star$ is the critical value of the parameter p that separates initial data that form a black hole (supercritical) from initial data that do not form a black hole (subcritical). Choptuik observed that the critical exponent γ_M is independent of the initial data chosen—the critical behavior is universal. The currently accepted value of the critical exponent is $\gamma_M = 0.374 \pm 0.001$ [2]. Not much later, Garfinkle and Duncan [3] discovered that in subcritical evolutions the maximum absolute value of the Ricci scalar at the center of the collapse obeys the scaling relation

$$R_{\rm max} \propto \left| \frac{p}{p_\star} - 1 \right|^{2\gamma_{R_{\rm max}}}. \tag{2}$$

Interestingly, $\gamma_{R_{\rm max}}$ was found to have the same value as γ_M.

Another key aspect of the critical behavior observed by Choptuik is that of a discretely self-similar solution, or "echoing." In the strong-field regime near the critical

solution, Choptuik noticed that any gauge-invariant quantity U obeys the relation

$$U(\mathcal{T}, x^i) = U(e^\Delta \mathcal{T}, e^\Delta x^i), \tag{3}$$

where Δ is a dimensionless constant. Here $\mathcal{T} = \tau - \tau_\star$, where τ is the proper time of a central observer and $\tau_\star$ is the value of τ when a naked singularity forms in the limit $p \to p_\star$. $\tau_\star$ is referred to as the accumulation time. As one moves closer in time to the critical solution by e^Δ, the same field profile is observed for U but at spatial scales e^Δ smaller. The echoing period Δ, like the critical exponent, is universal in the sense that it does not depend on the initial data, only on the type of matter undergoing gravitational collapse. The currently accepted value for a massless scalar field is $\Delta = 3.4453 \pm 0.0005$ [2].

Since the seminal work by Choptuik, many studies to better understand critical behavior in gravitational collapse have been performed. Studies of critical collapse of a massless scalar field in spherical symmetry have found that the critical exponent and echoing period are both independent of the initial data profile but depend on the dimensionality of the spacetime [4–7]. Similar studies observed that the critical exponent, echoing period, and possibly even the type of phase transition are changed in modified theories of gravity [8,9]. Interestingly, the presence of critical behavior appears to be independent of the matter source, but the value of the critical exponent, echoing period, and type of phase transition depend on the type of matter [10–17]. Vacuum critical collapse was first studied in [18,19], which found that critical behavior is present and that the critical exponent and echoing period have values different from those found in simulations with matter. Unfortunately, studying vacuum gravitational collapse has proven to be quite difficult [20–23].

---

*nd357@cornell.edu

In critical collapse the phase transition is either type I or type II. In type II phase transitions the black hole mass continuously goes to zero as $p_\star$ is approached. This has been the most common case observed so far when studying critical collapse. In type I transitions the mass of the black hole that forms approaches a constant, nonzero value as $p_\star$ is approached. Type I phase transitions have been clearly identified in critical collapse of a massive scalar field [12]. The discussion in this paper is only relevant for type II critical behavior.

In 1997 both Gundlach [2] and Hod and Piran [24] independently discovered fine structure in addition to the power-law behavior of the black hole masses: there is a small-amplitude modulation of (1). Specifically, the scaling relation is altered to

$$\ln(M_{\mathrm{BH}}) = \gamma_M \ln|p/p_\star - 1| + C$$
$$+ A\sin(w\ln|p/p_\star - 1| + \delta), \quad (4)$$

where C, A, w, and δ are constants. These authors predicted and verified that $w = \Delta/(2\gamma_M)$ for massless scalar field collapse in spherical symmetry. Whether or not this relation holds for different matter sources and beyond spherical symmetry is an open question.

Unfortunately, answering the question of how symmetry assumptions affect the critical exponent and echoing period has turned out to be quite challenging. The reason is that spatiotemporal scales varying over four to six orders of magnitude must be resolved in order to properly study the fine structure and echoing, and a large number of high-resolution simulations are necessary. In addition, the well-posedness and stability of the formulation of the Einstein equations solved and the choice of gauge have proven to be as problematic here as in other simulations in numerical relativity. Akbarian and Choptuik [25] have recently studied how formulations of the Einstein equations commonly used for binary black hole mergers behave when studying critical collapse. However, that work was restricted to spherical symmetry.

Critical collapse of a massless scalar field in axial symmetry was studied using perturbation theory by Martin-Garcia and Gundlach [26], who found that all nonspherical modes decay. In 2003 Choptuik *et al.* [27] performed numerical simulations of massless scalar field collapse in axial symmetry. They found that the critical solution in this case is the same as the solution found in spherical symmetry. However, in contrast to [26], they also found tentative evidence for a nondecaying $l = 2$ mode. More recently, Healy and Laguna [28] studied critical collapse of a massless scalar field that is symmetric about the xz-plane. Healy and Laguna observed results consistent with spherically symmetric collapse, but were unable to verify the echoing of gauge-independent fields. The work of Healy and Laguna has been followed by a study of massless scalar field collapse with a quartic potential by

Clough and Lim [29]. Clough and Lim also studied initial data similar to that of [28] and obtained results similar to those of Healy and Laguna.

In this paper we present a study of critical collapse of a massless scalar field with no symmetry assumptions, and the first study beyond spherical symmetry that is able to resolve the fine structure in the black hole mass scaling relation. We are able to resolve small-scale dynamics in both supercritical and subcritical evolutions, allowing us to directly compare the results. In Sec. II we review the equations solved, in Sec. III we discuss the initial data used, in Sec. IV we provide details about the numerical method, in Sec. V we present the results, and we conclude in Sec. VI.

Recently, a paper by Baumgarte appeared [30] in which axially symmetric initial data similar to that of [27] are studied. We discuss the relation between this paper and our work at the end of Sec. V.

II. EQUATIONS

We study the dynamics near the critical solution in gravitational collapse of the Einstein-Klein-Gordon system. We solve the Einstein equations,

$$R_{ab} = 8\pi\left(T_{ab} - \frac{1}{2}\psi_{ab}T^c{}_c\right) \quad (5)$$

where R_{ab} is the Ricci tensor, ψ_{ab} the spacetime metric, and T_{ab} the stress tensor. Here and throughout the rest of the paper we will use latin indices at the beginning of the alphabet, e.g., $a, b, c, \ldots$, to refer to spacetime indices running from 0 to 3, and later indices, $i, j, k, \ldots$, to refer to spatial indices running from 1 to 3. We use the ADM form of the metric,

$$ds^2 = -N^2 dt^2 + g_{ij}(N^i dt + dx^i)(N^j dt + dx^j) \quad (6)$$

where $N(t, x^i)$ is the lapse, $N^j(t, x^i)$ the shift, and $g_{ij}(t, x^k)$ the spatial metric. We denote the timelike unit normal orthogonal to the spacelike hypersurfaces by

$$t^a = (N^{-1}, -N^i/N). \quad (7)$$

We solve Eq. (5) using a first-order generalized harmonic (GH) formulation [31].

The matter source is a massless scalar field φ with

$$T_{ab} = \partial_a\varphi\partial_b\varphi - \frac{1}{2}\psi_{ab}\psi^{cd}\partial_c\varphi\partial_d\varphi. \quad (8)$$

To bring the resulting equations of motion into first-order form, we define the auxiliary variables $\Phi_i = \partial_i\varphi$ and $\Phi_{iab} = \partial_i\psi_{ab}$, and the conjugate variables $\Pi = -N^{-1}(\partial_t\varphi - N^i\partial_i\varphi)$ and $\Pi_{ab} = -N^{-1}(\partial_t\psi_{ab} - N^i\Phi_{iab})$.

The first-order GH system is [31]

$$\partial_t \psi_{ab} - (1 + \gamma_1) N^k \partial_k \psi_{ab} = -N\Pi_{ab} - \gamma_1 N^i \Phi_{iab}, \quad (9)$$

$$\begin{aligned}
\partial_t \Pi_{ab} &- N^k \partial_k \Pi_{ab} + N g^{ki} \partial_k \Phi_{iab} - \gamma_1 \gamma_2 N^k \partial_k \psi_{ab} \\
&= 2N\psi^{cd}(g^{ij}\Phi_{ica}\Phi_{jdb} - \Pi_{ca}\Pi_{db} - \psi^{ef}\Gamma_{ace}\Gamma_{bdf}) \\
&\quad - 2N\nabla_{(a}H_{b)} - \frac{1}{2}Nt^c t^d \Pi_{cd}\Pi_{ab} - Nt^c \Pi_{ci} g^{ij}\Phi_{jab} \\
&\quad + N\gamma_0 (2\delta^c_{\ (a}t_{b)} - \psi_{ab}t^c)(H_c + \Gamma_c) \\
&\quad - \gamma_1 \gamma_2 N^i \Phi_{iab} - 16\pi N\left(T_{ab} - \frac{1}{2}\psi_{ab}T^c_{\ c}\right), \quad (10)
\end{aligned}$$

$$\begin{aligned}
\partial_t \Phi_{iab} &- N^k \partial_k \Phi_{iab} + N\partial_i \Pi_{ab} - N\gamma_2 \partial_i \psi_{ab} \\
&= \frac{1}{2}Nt^c t^d \Phi_{icd}\Pi_{ab} + Ng^{jk}t^c \Phi_{ijc}\Phi_{kab} - N\gamma_2 \Phi_{iab}, \quad (11)
\end{aligned}$$

where H_a is the so-called gauge source function and must satisfy the constraint $H_a = \psi_{ab}\Gamma^b_{cd}\phi^{cd}$. The parameters γ_0, γ_1 and γ_2 are described in Sec. IV D. The first-order massless-Klein-Gordon system is

$$\partial_t \psi = N^i \partial_i \psi - N\Pi + \gamma_1^{KG} N^i (\partial_i \psi - \Phi_i), \quad (12)$$

$$\begin{aligned}
\partial_t \Pi &= N\Pi K + N^i \partial_i \Pi + N\Phi_i g^{jk}\Gamma^i_{jk} \\
&\quad + \gamma_1^{KG}\gamma_2^{KG} N^i (\partial_i \psi - \Phi_i) - g^{ij}(N\partial_j \Phi_i + \Phi_j \partial_i N),
\end{aligned}$$
$$(13)$$

$$\begin{aligned}
\partial_t \Phi_i &= -N\partial_i \Pi - \Pi\partial_i N - \gamma_2^{KG} N(\Phi_i - \partial_i \psi) \\
&\quad + N^j \partial_j \Phi_i + \Phi_j \partial_i N^j. \quad (14)
\end{aligned}$$

The parameters γ_1^{KG} and γ_2^{KG} are described in Sec. IV D, and K is the trace of the extrinsic curvature.

III. INITIAL DATA

We generate initial data for the evolutions by solving the extended conformal thin-sandwich equations [32] using the spectral elliptic solver [33] in SpEC [34]. The contributions to the equations from the scalar field are given by

$$\rho = t^a t^b T_{ab} = \frac{1}{2}(\Pi^2 + g^{ij}\Phi_i \Phi_j), \quad (15)$$

$$S^i = -g^{ij}t^a T_{aj} = g^{ij}\Pi\Phi_j, \quad (16)$$

and

$$S = g_{ij}g^{ia}g^{jb}T_{ab} = \frac{1}{2}(3\Pi^2 - g^{ij}\Phi_i \Phi_j), \quad (17)$$

where g^{ia} projects the spacetime index a onto the spatial hypersurface orthogonal to t^a.

Let $r = \delta_{ij}x^i x^j$ and

$$f(r) = \varphi_0 \exp\left[-\left(\frac{r - r_0}{\sigma}\right)^2\right]. \quad (18)$$

For concreteness we focus on three types of initial data: spherically symmetric data given by

$$\varphi(t, x^i) = \varphi_{\text{sph}} = \frac{f(-r) + f(r)}{r}, \quad (19)$$

data where the second term has no y-coordinate dependence (recall $xz \sim r\cos\phi\sin 2\theta$) similar to that studied in [28,29]

$$\varphi(t, x^i) = \varphi_{\Re(Y_1^2)} := \varphi_{\text{sph}}(1 - \delta\cos\phi\sin 2\theta), \quad (20)$$

and finally generic initial data of the form

$$\begin{aligned}
\varphi(t, x^i) = \varphi_{3-d} := \varphi_{\text{sph}}\Big\{ 1 &- \frac{\delta}{1.56}[(\cos\phi + \sin\phi)\sin 2\theta \\
&- (3\cos^2\theta - 1)] \Big\}. \quad (21)
\end{aligned}$$

The conjugate momentum to the φ in the spherically symmetric case is given by

$$\Pi_{\text{sph}} = \frac{\partial_r f(-r) - \partial_r f(r)}{r}, \quad (22)$$

and is multiplied by the same nonspherical terms as φ. These are ingoing spherical wave initial data. The numerical factor 1.56 is chosen so that when $\delta = 1$, the maximum of the second term is approximately unity. We choose $\sigma = 1$ and $r_0 = 5$ for the results presented here. For the initial data (20) we (arbitrarily) choose $\delta = 0.9$ and for data given by (21) we choose $\delta = 1$.

IV. NUMERICAL METHODS

A. Domain decomposition

SpEC decomposes the computational domain into possibly overlapping subdomains. Within each subdomain a suitable set of basis functions that depends on the topology of the subdomain is chosen to approximate the solution. The domain decomposition for finding the initial data is a cube at the center with an overlapping spherical shell that is surrounded by concentric spherical shells. For the evolution, a filled sphere surrounded by nonoverlapping spherical shells is used until a black hole forms. At this point a ringdown or excision grid nearly identical to that used during the ringdown phase of binary black hole merger evolutions is used [35–37]. The ringdown grid consists of a set of nonoverlapping spherical shells with the inner shell's

inner radius approximately 94% of the apparent horizon radius.

B. Dual frames and mesh refinement

To resolve the large range of spatial and temporal scales required, finite-difference codes typically use adaptive mesh refinement (AMR). However, for the spatiotemporal scales required here, AMR is computationally prohibitively expensive in $3 + 1$ dimensions without any symmetries.

SpEC achieves its high accuracy by using spectral methods to solve the partial differential equations (PDEs) rather than finite differencing. In addition, two further tools are employed to achieve high accuracy: dual frames [36–38] and spectral AMR [39].

In the dual frames approach, the PDEs are solved in what is called the grid frame. This frame is related to the "inertial frame," the frame in which the PDEs are originally written, by time-dependent spatial coordinate maps. The dual frames method "moves" the grid points inward as the scalar field collapses, which gives an additional two orders of magnitude of resolution compared to the initial inertial coordinates without the use of any mesh refinement. We also employ a coordinate map to slowly drift the outer boundary inward so that any constraint-violating modes near the outer boundary are propagated out of the computational domain. While the slow drift of the outer boundary is not essential for stability, it is helpful in long evolutions.

Denote the coordinate map that moves the grid points inward during collapse by $\mathcal{M}_{\text{scaling}}$ and the map that drifts the outer boundary inward by $\mathcal{M}_{\text{drift}}$. Then the coordinate map used during collapse before a black hole forms is given by $\mathcal{M}_{\text{collapse}} = \mathcal{M}_{\text{drift}} \circ \mathcal{M}_{\text{scaling}}$. The mapping $\mathcal{M}_{\text{collapse}}$ relates the initial coordinates $\bar{x}^i$ to the grid coordinates x^i by $\bar{x}^i = \mathcal{M}_{\text{collapse}} x^i$. The specific spatial coordinate map that we use for both $\mathcal{M}_{\text{drift}}$ and $\mathcal{M}_{\text{scaling}}$ is of the form

$$\bar{r} = a(t)r + [1 - a(t)]\frac{r^3}{r_{\text{outer}}^2}, \qquad (23)$$

where $r = \delta_{ij}x^i x^j$, $\bar{r} = \delta_{ij}\bar{x}^i \bar{x}^j$, $a(t)$ is a time-dependent function we call an expansion factor, and r_{outer} is a parameter of the map. For $\mathcal{M}_{\text{scaling}}$ we choose

$$a_{\text{scaling}}(t) = A \exp\left[-\left(\frac{t}{\sigma_{\text{scaling}}}\right)^{2n}\right] + B \qquad (24)$$

with $A = 0.99$, $B = 0.01$, $n = 2$ and $\sigma_{\text{scaling}} = 3.8$. The value of r_{outer} for $\mathcal{M}_{\text{scaling}}$ is $r_{\text{outer}} = 100$. For $\mathcal{M}_{\text{drift}}$ we use $r_{\text{outer}} = 180$ and

$$a_{\text{drift}}(t) = 1 + v\frac{t^3}{b + t^2}, \qquad (25)$$

with $b = 10^{-4}$ and $v = -3.23 \times 10^{-3}$. We find that these choices for the coordinate maps lead to accurate and stable

long-term evolutions with sufficient resolution to resolve both scaling and echoing.

After an apparent horizon is found we switch over to an excision grid and use the same coordinate maps used in the ringdown portion of the binary black hole evolutions [35–37]. Specifically, we excise the interior of the apparent horizon with the excision surface's radius being approximately 94% of the apparent horizon's coordinate radius. Near the apparent horizon, all the characteristics are directed toward the center of the apparent horizon and so no boundary conditions need to be imposed there. Thus, as long as the excision surface remains close to the apparent horizon, the simulation remains stable without the need to impose additional boundary conditions. One difficulty is that during the very early phase of ringdown the apparent horizon's coordinate radius increases very rapidly. To deal with the rapid expansion, a control system is used to track the apparent horizon and adjust the location of the excision boundary to follow the apparent horizon [35,37,38].

While the spatial coordinate maps work extremely well for resolving the small length scales that appear near the critical solution, they do not provide any guarantees about the truncation error of the simulations. The temporal error is controlled by using an adaptive, fifth-order Dormand-Prince time stepper. The spatial error is controlled using the spectral AMR algorithm described in [39]. Using AMR we control the relative error in the metric, the spatial derivative of the metric and the conjugate momentum of the metric. For the results presented in this manuscript we set a relative maximum spatiotemporal error of 10^{-8}.

C. Gauge choice

In binary black hole evolutions with the GH system, large constraint violations occur unless an appropriate gauge condition is chosen. The key ingredient in a successful choice [40] is to control the growth of $\sqrt{g}/N$, where g is the determinant of the spatial metric. As one might expect, evolutions of critical behavior at black hole formation require even more stringent control of the gauge than in binary simulations. We find that without such control, explosive growth in both $\sqrt{g}/N$ and $1/N$ prevents the code from finding an apparent horizon before the constraints blow up and the evolution fails. Accordingly, we adopt a modified version of the damped harmonic gauge used in Ref. [40]:

$$H_a = \left[\mu_{L,1}\log\left(\frac{\sqrt{g}}{N}\right) + \mu_{L,2}\log\left(\frac{1}{N}\right)\right]t_a - \mu_S N^{-1}g_{ai}N^i.$$
$$(26)$$

The coefficients $\mu_{L,1}$, $\mu_{L,2}$ and μ_S are described below.

Fortunately, the region of the spatial hypersurfaces where $\sqrt{g}/N$ diverges is different from that where $1/N$ diverges and so having the coefficients $\mu_{L,1}$ and $\mu_{L,2}$ depend

on $\log(\sqrt{g}/N)$ and $\log 1/N$ respectively allows us to control both divergences with a single equation. The functional forms of the coefficients are

$$\mu_{L,1} = R(t)W(x^i)\left[\log\left(\frac{\sqrt{g}}{N}\right)\right]^4, \tag{27}$$

$$\mu_{L,2} = R(t)W(x^i)\left[\log\left(\frac{1}{N}\right)\right]^4, \tag{28}$$

and

$$\mu_S = \mu_{L,1}. \tag{29}$$

The roll-on function $R(t)$ is given by

$$R(t) = 1 - \exp\left[-\left(\frac{t-t_0}{\sigma_t}\right)^4\right], \tag{30}$$

where we choose $t_0 = 0$ and $\sigma_t = 2$, while the spatial weight function $W(x^i)$ is given by

$$W(x^i) = \exp\left[-34.54\left(\frac{r}{r_{\max}}\right)^2\right], \tag{31}$$

where we set $r_{\max} = 30$. The function $R(t)$ is used to transition from the initial maximal slicing to the damped harmonic gauge needed later in the evolution, while $W(x^i)$ makes the gauge be pure harmonic near the outer boundary of the computational domain. The log factors in Eqs. (27) and (28) make the gauge pure harmonic in the region of the spatial slice where $\sqrt{g}/N$ and $1/N$ are near unity, respectively. We found that using the fourth power as opposed to the second power that is typically used for controlling the growth of $\sqrt{g}/N$ in binary black hole evolutions is required for stable long-term evolutions.

D. Constraint damping

Both the Klein-Gordon and the GH system have constraints that must remain satisfied during evolutions. For the Klein-Gordon system the constraint is

$$\mathcal{C}_i^{KG} = \partial_i\psi - \Phi_i = 0. \tag{32}$$

The constraints for the GH system are given in Ref. [31].

Failure to satisfy the constraints indicates that the numerical simulation is no longer solving the physical system of interest and should not be trusted. To control the growth of constraint violations from numerical inaccuracies, constraint damping parameters are added to the evolution equations. For the GH system the constraint damping parameters are γ_0, γ_1 and γ_2, and for the Klein-Gordon system γ_1^{KG} and γ_2^{KG}. See Eqs. (9)–(14) for how the constraint damping parameters appear in the evolution

equations. We find that choosing $\gamma_1^{KG} = 1$ and $\gamma_2^{KG} = 0$ works well for the scalar field. For the GH system, finding good constraint damping parameters is more difficult, especially during ringdown. The dimensions of the constraint damping parameters are time^{-1}, which suggests that for smaller black holes where the characteristic time scale is shorter, the constraint damping parameters must be increased. During ringdown we choose

$$\gamma_0 = A_0 \exp\left(-\frac{r^2}{10^2}\right) + 10^{-3}, \tag{33}$$

$$\gamma_1 = A_1\left[\exp\left(-\frac{r^2}{1000^2}\right) - 1\right], \tag{34}$$

$$\gamma_2 = A_2 \exp\left(-\frac{r^2}{10^2}\right) + 10^{-3}, \tag{35}$$

with $A_0 \in [20, 100]$, $A_1 = 0.999$, and $A_2 \in [20, 80]$. Larger values of A_0 and A_2 are used for smaller black holes. During the collapse phase of the evolutions we find less sensitivity to the choice of the damping parameters. We use the same functional form as during the ringdown but always choose $A_0 = A_2 = 20$.

V. RESULTS

All files used to produce figures in this paper, including the data, are available from the arXiv version of this paper.

A. Scaling

In this section we present two sets of scaling relations. The first involves the final mass of the black hole M_{BH} for supercritical evolutions. For each class of initial data we evolve the data with amplitudes large enough that a black hole forms and gradually decrease the amplitude. While decreasing the amplitude we focus on simulations that form a black hole. Rather than performing a binary search to estimate $p_\star$, we fit the relationship $\ln(M_{BH}) = \gamma \ln(p/p_\star - 1) + C$ to the data for γ, $p_\star$, and C, where we take p to be the amplitude φ_0 of the initial data. We then use the $p_\star$ from the fit to determine an amplitude that should form a black hole but is closer to the critical solution. This is repeated until $\log_{10}(p/p_\star - 1) \approx -6$, the target value. Choosing suitable values of p to fit for γ and Δ is tricky. We describe our procedure in the Appendix. Note that the relationship used for determining which amplitude to use next is not used for analyzing the results.

The second scaling relation involves $R_{\max}$, the maximum Ricci scalar at the center for subcritical evolutions. We run simulations to obtain an approximately even distribution of masses and maximum Ricci scalars for $\ln(p/p_\star - 1) \in (-14, -5]$. We estimate the errors in the final mass of the

black hole and R_{max} using convergence tests with values of p nearest $p_\star$.

Once we have reached the target number of simulations, with the lowest amplitude that forms a black hole having $\log_{10}(p/p_\star - 1) \approx -6$, we fit the mass of the resulting black hole to

$$\ln(M_{\mathrm{BH}}) = \gamma^M \ln(p/p_\star - 1) + C^M \\ + A^M \sin[w^M \ln(p/p_\star - 1) + \delta^M], \quad (36)$$

as suggested in [2,24]. Note that the superscript M is not an exponent but denotes that parameter was obtained from fitting to the mass of the black hole rather than the maximum Ricci scalar at the center. We find that the probability of χ^2 and the reduced χ^2 are better for this function than the one where the sinusoidal term is omitted. We fit for all parameters in (35), including $p_\star$. The fitting function used for the maximum Ricci scalar at the origin is

$$\ln(R_{\mathrm{max}}) = 2\gamma^R \ln(p/p_\star - 1) + C^R \\ + A^R \sin[w^R \ln(p/p_\star - 1) + \delta^R]. \quad (37)$$

However, for consistency we use the value of $p_\star$ obtained from fitting to the masses when fitting to the maximum Ricci scalar as well.

In Fig. 1 we plot $\ln(M_{\mathrm{BH}})$ as a function of $\ln(p/p_\star - 1)$ for the three types of initial data studied. For data $\varphi_{\Re(Y_1^2)}$ we arbitrarily choose $\delta = 0.9$, which is a large deviation from the spherical solution. For reference, when $\delta = 1$ the scalar field profile is zero at the zeros of $1 - \cos(\varphi)\sin(2\theta)$.
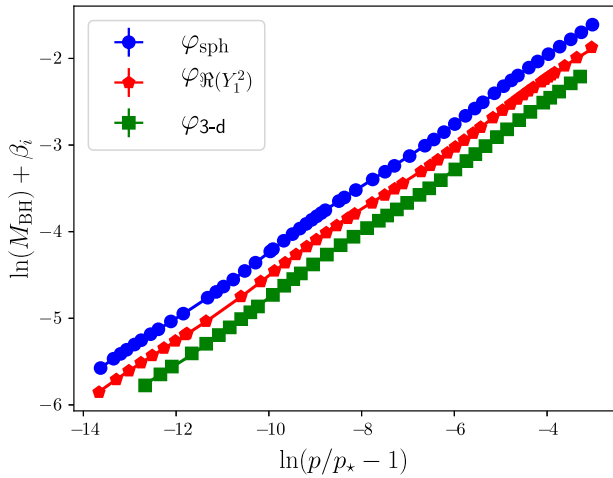
For initial data $\varphi_{\text{3-d}}$ we choose $\delta = 1$, an even stronger deviation from spherical symmetry. In Fig. 1 we offset the curves vertically by $\beta_i = \{0.3, 0, -0.3\}$ so that they do not overlap and are easier to compare. The critical exponents we find are $\gamma^M_{\mathrm{sph}} = 0.3753(1)$, $\gamma^M_{\Re(Y_1^2)} = 0.3748(2)$, and $\gamma^M_{\text{3-d}} = 0.3761(3)$, where the number in parentheses is the uncertainty in the last digit. These are all close to the accepted value for spherically symmetric initial data, 0.374 ± 0.001 [2], strongly suggesting that the spherical mode dominates.

In addition to studying the final mass of the resulting black hole, we follow [3] and calculate the maximum Ricci scalar at the center of the collapse for subcritical evolutions. In Fig. 2 we plot $\ln(R_{\mathrm{max}})$ as a function of $\ln(p/p_\star - 1)$ along with a fit using Eq. (37) for the initial data studied. We again offset the plots vertically by amounts $\beta_i = \{0.4, 0, -0.4\}$ to aid readability. In this case we find critical exponents $\gamma^R_{\mathrm{sph}} = 0.3787(1)$, $\gamma^R_{\Re(Y_1^2)} = 0.3761(1)$, and $\gamma^R_{\text{3-d}} = 0.3755(2)$, which are comparable to the values for mass scaling and to the accepted value in spherically symmetric critical collapse, $\gamma = 0.374 \pm 0.001$.

B. Echoing

Having studied the scaling we now turn to the fine structure and echoing of the critical behavior. Echoing of any gauge-invariant quantity was described by Eq. (3) above. A small-amplitude sinusoidal modulation about the straight line expected from critical behavior was conjectured and observed in [24]. Figures 1 and 2 both show this feature. In Fig. 3 we plot the residuals when fitting only the linear term and when fitting the linear plus sine term for the
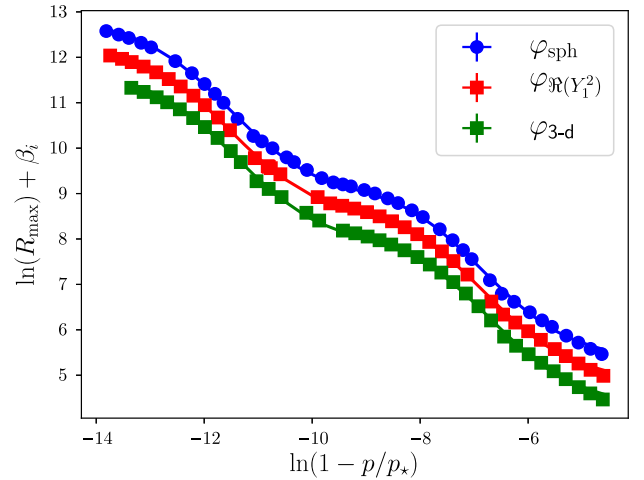

FIG. 1. $\ln(M_{\mathrm{BH}})$ plotted as a function of $\ln(p/p_\star - 1)$ for the three types of initial data studied. We find critical exponents $\gamma^M_{\mathrm{sph}} = 0.3753(1)$, $\gamma^M_{\Re(Y_1^2)} = 0.3748(2)$, and $\gamma^M_{\text{3-d}} = 0.3761(3)$. We shift the curves vertically by $\beta_i = \{0.3, 0, -0.3\}$ so that data points from different initial data are easily distinguished.
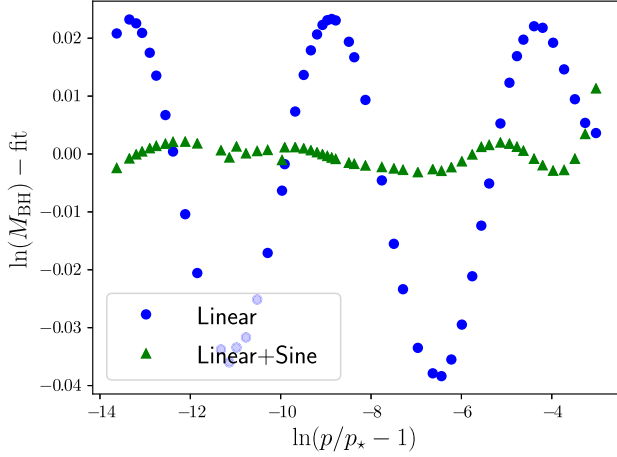

FIG. 2. $\ln(R_{\mathrm{max}})$ plotted as a function of $\ln(1 - p/p_\star)$ for the three types of initial data studied. We find critical exponents $\gamma^R_{\mathrm{sph}} = 0.3787(1)$, $\gamma^R_{\Re(Y_1^2)} = 0.3761(1)$, and $\gamma^R_{\text{3-d}} = 0.3755(2)$. We shift the curves vertically by $\beta_i = \{0.4, 0, -0.4\}$ so that data points from different initial data are easily distinguished.

FIG. 3. The residuals of the fitting $\ln(M_{\mathrm{BH}}) = \gamma^M \ln(p/p_\star - 1) + C$ (blue dots) and Eq. (36) (green triangles) to the black hole masses for the spherical symmetry case, φ_{sph}. The sinusoidal residual of the straight line fit is identical to what is observed in [24].
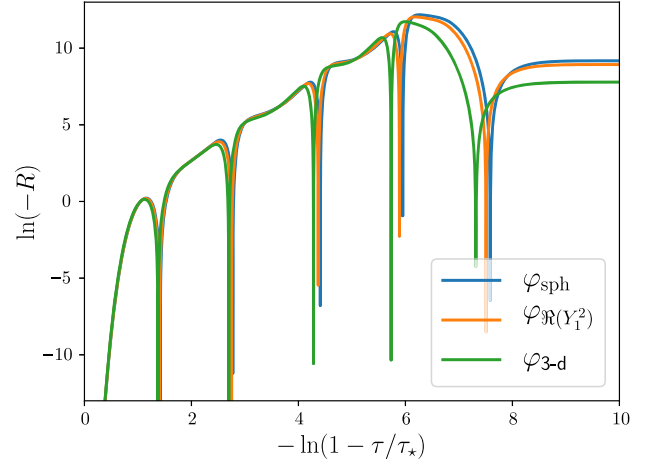

FIG. 4. $\ln(R(t, r = 0))$ plotted as a function of $\ln(1 - \tau/\tau_\star)$ for the three types of initial data studied. The echoing is clearly visible and very similar between the different evolutions, which all have $\ln(1 - p/p_\star) \approx -6$. The echoing period is $\Delta = 3.2 \pm 0.1$ for all simulations.

spherically symmetric mass scaling case.[1] The sinusoidal modulation is much clearer in Fig. 3 than in Fig. 1.

From the fit, Eq. (36), we estimate the period, $T = 2\pi/w$. In [24] it was found that the relationship between the echoing period Δ and the scaling period T is $T = \Delta/(2\gamma)$. To test this relationship, we calculate Δ using T and also by estimating it directly from the Ricci scalar at the origin as a function of the logarithmic time, $-\ln(1 - \tau/\tau_\star)$. τ is the proper time at the origin given by

$$\tau = \int_0^t N(\tilde{t}, 0)d\tilde{t}, \qquad (38)$$

and $\tau_\star$ is the accumulation time of the self-similar solution.

We find that despite being able to resolve the fine structure and knowing $p_\star$ to six significant figures, the estimate of $\tau_\star$ from the apparent horizon formation time is only accurate to about two digits. This is because the formation time of an apparent horizon is a gauge-dependent quantity. We estimate $\tau_\star$ by assuming that the logarithmic time between successive echoes becomes constant and adjusting $\tau_\star$ until this is true. The resulting $\tau_\star$ is consistent with what we estimate from apparent horizon formation times. In Fig. 4 we plot $\ln(R(t, r = 0))$, a geometric invariant, which shows the expected echoing that has been studied in previous works [3,6]. From Fig. 4 we estimate the echoing period to be $\Delta = 3.2 \pm 0.1$.

In Table I we summarize and compare direct estimates of Δ to $2\gamma T$. Specifically, we find that $2\gamma^M T^M \approx 3.46$, near the best known value of $\Delta = 3.4453 \pm 0.0005$ [2]. For simulations that do not form a horizon, where we compute

$2\gamma^R T^R$ from the Ricci scalar scaling plot, Fig. 2, we find that $2\gamma^R_{\mathrm{sph}} T^R_{\mathrm{sph}} = 3.556 \pm 0.001$, $2\gamma^R_{\Re(Y_1^2)} T^R_{\Re(Y_1^2)} = 3.518 \pm 0.002$, and $2\gamma^R_{\text{3-d}} T^R_{\text{3-d}} = 3.512 \pm 0.003$. The discrepancy between $2\gamma T$ from mass scaling and Ricci scalar scaling is currently not understood. When studying the echoing of $\ln(-R(t, r = 0))$, we find $\Delta = 3.2 \pm 0.1$, where the larger error is explained by the difficulty in estimating $\tau_\star$.

A power spectrum analysis shows that the spherical mode dominates the evolution. We define the power in a given ℓ-mode as

$$P_\ell = \frac{1}{N_r} \sum_{i=0}^{N_r-1} \sum_{m=-\ell}^{\ell} |C_{i,\ell,m}|^2 \qquad (39)$$

where N_r is the number of radial points, and $C_{i,\ell,m}$ are the coefficients in spectral expansion. This definition is consistent with Parseval's theorem given that

$$\int |Y_m^\ell(\theta, \phi)|^2 d\Omega = 1. \qquad (40)$$

Also note that with this definition at a given radius

TABLE I. Comparison of $2\gamma^M T^M$ and the echoing period Δ. In [24] it was found that $\Delta = 2\gamma T$, which we are unable to verify within our error estimates. The accepted value of the echoing period in spherical symmetry is $\Delta = 3.4453 \pm 0.0005$ [2].

Initial data	$2\gamma^M T^M$	$2\gamma^R T^R$	$\Delta_{\mathrm{echoing}}$
φ_{sph}	3.46 ± 0.01	3.557 ± 0.001	3.2 ± 0.1
$\varphi_{\Re(Y_1^2)}$	3.46 ± 0.02	3.518 ± 0.002	3.2 ± 0.1
$\varphi_{\text{3-d}}$	3.67 ± 0.04	3.512 ± 0.003	3.2 ± 0.1

---

[1]The residuals of the fits for nonspherical initial data and for Ricci scaling are qualitatively identical.

$$\int |f(\theta,\phi)|^2 d\Omega = \sum_{\ell=0}^{\infty} P_\ell. \tag{41}$$

For the $\Re(Y_1^2)$ data we find that initially

$$\frac{P_2}{P_0} = \frac{27}{125} \Rightarrow \frac{P_2}{\sum_\ell P_\ell} = \frac{P_2}{P_0 + P_2} \approx 0.18, \tag{42}$$

or that approximately 18% of the power is in the $\ell = 2$ mode. For the 3D initial data we find that initially

$$\frac{P_2}{P_0} \approx 0.548 \Rightarrow \frac{P_2}{\sum_\ell P_\ell} = \frac{P_2}{P_0 + P_2} \approx 0.35, \tag{43}$$

or that approximately 35% of the power is in the $\ell = 2$ mode.

In Fig. 5 we plot the power in φ_ℓ for $\ell = 0, 2$ for the $\Re(Y_1^2)$ initial data. Figure 5 shows that the $\ell = 2$ mode decays much more rapidly than the $\ell = 0$ mode, suggesting that the spherically symmetric critical solution is approached. However, given the different initial data and that we are further from the critical solution than [27], we are unable to corroborate or dispute their results.

The initial data used in [30] are given by

$$\varphi_{Y_2^2} = \varphi_0 \exp\left(-\frac{r}{r_0}\right)[\sin^2\theta + (1-\delta^2)\cos^2\theta]$$

$$= \varphi_0 \exp\left(-\frac{r}{r_0}\right)(1-\delta^2+\delta^2\sin^2\theta). \tag{44}$$

The deformation in this case is proportional to the $Y_2^{\pm 2}$ spherical harmonics as opposed to the Y_2^1 spherical harmonic. The author of Ref. [30] found that for $\delta = 0.75$ the critical behavior differs significantly from that of the spherically symmetric evolutions. For example, the critical exponent is observed to be $\gamma \approx 0.306$. The percentage of the
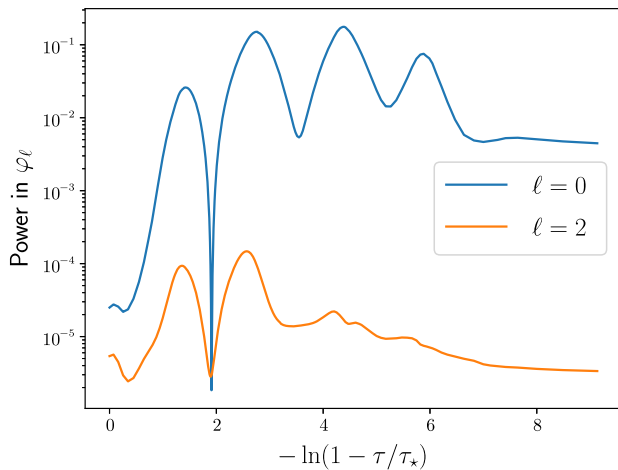

FIG. 5. The power in φ_ℓ for $\ell = 0, 2$ for the $\Re(Y_1^2)$ initial data with $\varphi_0 = 0.07586803$.

power in the $\ell = 2$ mode for $\delta = 0.75$ is approximately 47%. This is 12% more than our 3D initial data that has behavior consistent with the spherically symmetric evolutions. This raises the question as to whether the reason [30] we see different behavior is because of the increased power in the $\ell = 2$ modes or because the initial data are proportional to the $Y_2^{\pm 2}$ spherical harmonics instead of the Y_2^1 spherical harmonic. Work is under way to attempt to resolve this question.

VI. CONCLUSIONS

We present the results of a study of critical behavior in the 3D gravitational collapse of a massless scalar field with no symmetry assumptions. We are able to resolve the dominant critical behavior as well as the fine structure in both supercritical and subcritical evolutions. We use the Spectral Einstein Code, SpEC [34], to perform the evolutions, with several key changes to the gauge condition and constraint damping. We study how the critical exponent and echoing period obtained from the data depend on how close to the critical solution the simulations are, as well as how the simulations are distributed in parameter space. This is especially important in 3D where simulations are costly to perform. We find the critical exponents to be $\gamma_{\text{sph}}^M = 0.3753(1)$, $\gamma_{\Re(Y_1^2)}^M = 0.3748(2)$, and $\gamma_{\text{3-d}}^M = 0.3761(3)$, consistent with the accepted result in spherical symmetry of 0.374 ± 0.001 [2]. The accepted value of the echoing period Δ in spherical symmetry is $\Delta = 3.4453 \pm 0.0005$ [2], while we find echoing periods $\Delta = 3.2 \pm 0.1$ for all initial data considered. The discrepancy can be attributed to the difficulty in directly measuring the echoing period. We also test the predicted relationship [2,24] between the echoing period and the fine structure of the scaling, $2\gamma T = \Delta$. We find that for mass scaling $2\gamma_{\text{sph}}^M T_{\text{sph}}^M = 3.46 \pm 0.01$, $2\gamma_{\Re(Y_1^2)}^M T_{\Re(Y_1^2)}^M = 3.46 \pm 0.02$, and $2\gamma_{\text{3-d}}^M T_{\text{3-d}}^M = 3.67 \pm 0.04$, where T^M is the period of the sinusoidal fine structure.

The agreement of the critical exponent, echoing period, and fine structure between the spherically symmetric and highly nonspherical simulations leads us to conclude that even for initial data far from spherical symmetry the critical solution is that of spherical symmetry. However, the reason why our results differ from those of [27,30], where data far from spherical symmetry approach a different critical solution, is not yet fully understood. One reason for the discrepancy could be that in our data approximately 18% of the total power is in the $\ell = 2$ mode for the $\Re(Y_1^2)$ initial data and 35% for the $3 - d$ initial data, while in [30] approximately 47% of the power is in the $\ell = 2$ mode. In other words, more power than we used is needed in the $\ell = 2$ mode. Another possible reason is that the author of Ref. [30] studied $\ell = 2, m = 2$ initial data while we study $\ell = 2, m = 1$ initial data. Work is under way to understand if either of these scenarios are responsible for the

discrepancy and to independently reproduce the simulations of [30].

APPENDIX: CHOOSING PARAMETER VALUES FOR SIMULATIONS

When estimating the error in the critical exponent γ and $2\gamma T$, we find it important to not only consider the error obtained from convergence tests, but also to study how γ and $2\gamma T$ depend on the number of data points, and how close to $p_\star$ the data points are. The former should be thought of as whether or not the $\ln(p - p_\star)$ space is sampled densely enough by the simulations. While reducing this error requires more (potentially costly) simulations, these simulations will be similar in their dynamics to simulations that have already been performed and so no algorithmic changes to the code are generally required. Determining how the closeness to $p_\star$ affects γ and $2\gamma T$ is a closely related, but separate issue. We study both of these sources of errors separately, while error estimates from convergence tests are included as error bounds on M_{BH} in the fits.

We use two methods to estimate the errors from our sampling of the $\ln(p - p_\star)$ space. First, we use bootstrapping to study how choosing different data points from within the data sets alters the critical exponent and $2\gamma T$. Second, we build a minimal grid that achieves the desired error tolerances by using a greedy algorithm. If the minimal grid is the same as or quite close to our grid we deduce that our grid may not be sufficiently dense to accurately extract γ and $2\gamma T$. We will now outline these methods in more detail.

The goal of bootstrapping is to resample the data set randomly to obtain knowledge about how well the data set represents the full population. This is done by randomly selecting as many points as there are in the data set, while allowing repetition. Equation (36) is then fit to the randomly selected points to obtain the critical exponent and $2\gamma T$. By repeating this procedure many times (we choose 10 000 times) we are able to plot a histogram of the critical exponents and values of $2\gamma T$. The variance in both

γ and $2\gamma T$ is then obtained by fitting a Gaussian to the histograms.

Using bootstrapping we find that the critical exponents obtained from mass scaling are left unchanged to within error with values $\gamma_{\mathrm{sph}}^M = 0.3753(2)$, $\gamma_{\Re(Y_1^2)}^M = 0.3750(5)$, and $\gamma_{\text{3-d}}^M = 0.376(1)$. For Ricci scaling, we find that the critical exponents also do not change within error, but the error estimate from bootstrapping is larger by approximately an order of magnitude than from the fit to the full data set. The values obtained for γ from Ricci scaling are $\gamma_{\mathrm{sph}}^R = 0.379(3)$, $\gamma_{\Re(Y_1^2)}^R = 0.376(3)$, and $\gamma_{\text{3-d}}^R = 0.375(5)$. For $2\gamma T$ we find qualitatively similar results to the critical exponent. Using data points from mass scaling we find $2\gamma_{\mathrm{sph}}^M T_{\mathrm{sph}}^M = 3.46 \pm 0.03$, $2\gamma_{\Re(Y_1^2)}^M T_{\Re(Y_1^2)}^M = 3.47 \pm 0.06$, and $2\gamma_{\text{3-d}}^M T_{\text{3-d}}^M = 3.7 \pm 0.8$ and from Ricci scaling we find $2\gamma_{\mathrm{sph}}^R T_{\mathrm{sph}}^R = 3.56 \pm 0.02$, $2\gamma_{\Re(Y_1^2)}^R T_{\Re(Y_1^2)}^R = 3.52 \pm 0.05$, and $2\gamma_{\text{3-d}}^R T_{\text{3-d}}^R = 3.51 \pm 0.07$.

A greedy algorithm is designed to find the approximate global minimum of a problem by selecting the path that is a local minimum at each node in the decision tree. In this case we seek the optimal values of p to determine γ and $2\gamma T$. Assume we have a minimal data set that allows the fitting procedure to succeed. Then the greedy algorithm randomly selects a new value of p and computes the corresponding black hole mass using Eq. (36). If adding the computed black hole mass to the data set decreases the error it is added; otherwise a new value of p is selected and added if it decreases the error in γ and $2\gamma T$. This is repeated until the error in γ and $2\gamma T$ is below some specified tolerance.

The greedy algorithm method takes as input a range of $\ln(p/p_\star - 1)$ in which to sample points, as well as the fit parameters obtained from a numerical study, i.e., $p_\star$, γ, C, A, w, and δ. Fake black hole masses are computed using (36) and adding a random offset of at most $\pm 10^{-3}$ to simulate numerical errors that would be present in the numerical simulations. The algorithm initially randomly chooses five (or six if also fitting for $p_\star$) data points on the specified interval of $\ln(p/p_\star - 1)$. Next, points are randomly added until the fitting algorithm successfully identifies fit parameters. Then data points are randomly chosen and added to the data set only if they reduce $|\gamma_{\mathrm{greedy}} - \gamma_{\mathrm{simulation}}|$. Data points are added until $|\gamma_{\mathrm{greedy}} - \gamma_{\mathrm{simulation}}| < 10^{-4}$.

Using the greedy algorithm, we find that for $\ln(p/p_\star - 1) \in [-14, -3]$ roughly 11 evenly spaced data points are necessary to achieve the desired tolerance and for $\ln(p/p_\star - 1) \in [-7, -3]$ approximately 15 evenly spaced data points are necessary. This is far fewer than the roughly 40 to 50 data points used for the fits to the numerical simulations. One reason for the difference in the number of data points is that, as indicated by the greedy algorithm results, initially when we do not know $p_\star$ very accurately a denser grid is necessary to obtain a fit of decent accuracy.

Another reason is that after finding $p_\star$ to some accuracy we performed simulations to fill a grid with a spacing of approximately 0.1 in $\log_{10}(p/p_\star - 1)$, which, in hindsight was unnecessary. Finally, a factor that was not accounted for in the greedy algorithm is that the fitting algorithm may not succeed because a good initial guess for the fit parameters is not known. The greedy algorithm always used the input that we modeled the data from.

To estimate the errors in γ and $2\gamma T$ arising from how far from criticality the simulations are, we fit to only the lower or upper 25%, 50% and 75% of data points. This provides insight into how many digits of the critical amplitude $p_\star$ need to be resolved for the fits to be reliable. We note that this test only determines whether or not γ and $2\gamma T$ are locally constant in $\ln(p - p_\star)$ space. The test cannot make any definitive statements about γ and $2\gamma T$ far outside this range, though this remains true regardless of how close to machine precision $1 - p_\star/p$ is.

By fitting to only a subset of the data set, we observe that when fewer than two to three significant figures of $p_\star$ are known, the linear + sine fit either fails to converge or else exhibits high sensitivity to the initial guess of the fitting parameters. However, the linear fit is still robust in this regime. Ultimately, we find that knowing $p_\star$ to five or more significant figures provides robust fit results and good accuracy of the local critical exponent and $2\gamma T$, while knowing $p_\star$ to fewer digits can lead to convergent fits that are biased by not having sufficiently resolved the sinusoidal oscillation.

[1] M. W. Choptuik, Phys. Rev. Lett. **70,** 9 (1993).
[2] C. Gundlach, Phys. Rev. D **55,** 695 (1997).
[3] D. Garfinkle and G. C. Duncan, Phys. Rev. D **58,** 064024 (1998).
[4] D. Garfinkle, C. Cutler, and G. C. Duncan, Phys. Rev. D **60,** 104007 (1999).
[5] J. Bland, B. Preston, M. Becker, G. Kunstatter, and V. Husain, Classical Quantum Gravity **22,** 5355 (2005).
[6] E. Sorkin and Y. Oren, Phys. Rev. D **71,** 124005 (2005).
[7] T. Taves and G. Kunstatter, Phys. Rev. D **84,** 044034 (2011).
[8] N. Deppe, C. D. Leonard, T. Taves, G. Kunstatter, and R. B. Mann, Phys. Rev. D **86,** 104011 (2012).
[9] S. Golod and T. Piran, Phys. Rev. D **85,** 104015 (2012).
[10] M. W. Choptuik, T. Chmaj, and P. Bizon, Phys. Rev. Lett. **77,** 424 (1996).
[11] C. Gundlach, Phys. Rev. D **55,** 6002 (1997).
[12] P. R. Brady, C. M. Chambers, and S. M. C. V. Goncalves, Phys. Rev. D **56,** R6057 (1997).
[13] D. Garfinkle, R. B. Mann, and C. Vuille, Phys. Rev. D **68,** 064015 (2003).
[14] T. W. Baumgarte and P. J. Montero, Phys. Rev. D **92,** 124065 (2015).
[15] C. Gundlach and T. W. Baumgarte, Phys. Rev. D **94,** 084012 (2016).
[16] T. W. Baumgarte and C. Gundlach, Phys. Rev. Lett. **116,** 221103 (2016).
[17] C. Gundlach and T. W. Baumgarte, Phys. Rev. D **97,** 064006 (2018).
[18] A. M. Abrahams and C. R. Evans, Phys. Rev. Lett. **70,** 2980 (1993).
[19] A. M. Abrahams and C. R. Evans, Phys. Rev. D **49,** 3998 (1994).
[20] E. Sorkin, Phys. Rev. D **81,** 084062 (2010).
[21] E. Sorkin, Classical Quantum Gravity **28,** 025011 (2011).
[22] D. Hilditch, T. W. Baumgarte, A. Weyhausen, T. Dietrich, B. Brügmann, P. J. Montero, and E. Mller, Phys. Rev. D **88,** 103009 (2013).
[23] D. Hilditch, A. Weyhausen, and B. Brügmann, Phys. Rev. D **93,** 063006 (2016).
[24] S. Hod and T. Piran, Phys. Rev. D **55,** R440 (1997).
[25] A. Akbarian and M. W. Choptuik, Phys. Rev. D **92,** 084037 (2015).
[26] J. M. Martin-Garcia and C. Gundlach, Phys. Rev. D **59,** 064031 (1999).
[27] M. W. Choptuik, E. W. Hirschmann, S. L. Liebling, and F. Pretorius, Phys. Rev. D **68,** 044007 (2003).
[28] J. Healy and P. Laguna, Gen. Relativ. Gravit. **46,** 1722 (2014).
[29] K. Clough and E. A. Lim, arXiv:1602.02568.
[30] T. W. Baumgarte, Phys. Rev. D **98,** 084012 (2018).
[31] L. Lindblom, M. A. Scheel, L. E. Kidder, R. Owen, and O. Rinne, Classical Quantum Gravity **23,** S447 (2006).
[32] H. P. Pfeiffer and J. W. York, Jr., Phys. Rev. D **67,** 044022 (2003).
[33] H. P. Pfeiffer, L. E. Kidder, M. A. Scheel, and S. A. Teukolsky, Comput. Phys. Commun. **152,** 253 (2003).
[34] http://www.black-holes.org/SpEC.html.
[35] M. A. Scheel, M. Boyle, T. Chu, L. E. Kidder, K. D. Matthews, and H. P. Pfeiffer, Phys. Rev. D **79,** 024003 (2009).
[36] B. Szilagyi, L. Lindblom, and M. A. Scheel, Phys. Rev. D **80,** 124010 (2009).
[37] D. A. Hemberger, M. A. Scheel, L. E. Kidder, B. Szilgyi, G. Lovelace, N. W. Taylor, and S. A. Teukolsky, Classical Quantum Gravity **30,** 115001 (2013).
[38] M. A. Scheel, H. P. Pfeiffer, L. Lindblom, L. E. Kidder, O. Rinne, and S. A. Teukolsky, Phys. Rev. D **74,** 104006 (2006).
[39] B. Szilgyi, Int. J. Mod. Phys. D **23,** 1430014 (2014).
[40] L. Lindblom and B. Szilagyi, Phys. Rev. D **80,** 084019 (2009).